Article

Genetic mixing and demixing on expanding spherical frontiers

Alba García Vázquez[1], Namiko Mitarai[1], and Liselotte Jauffred[1,*]

[1]The Niels Bohr Institute, University of Copenhagen, Blegdamsvej 17, DK-2100 Copenhagen O, Denmark
[*]Correspondence: jauffred@nbi.dk

Preprint server: BioRxiv
Classification: Physical Sciences, Biophysics and Computational Biology
Keywords: Biofilm, morphology, E. coli, range expansion, spatio-genetic patterning, 3D growth

ABSTRACT Genetic fluctuation during range expansion is a key process driving evolution. When a bacterial population is expanding on a two-dimensional (2D) surface, random fluctuations in the growth of the pioneers at the front line cause a strong de-mixing of genotypes. Even when there is no selective advantage (e.g., isogenetic strains apart from fluorescent plasmids), sectors of low genetic diversity are formed. Experimental studies of range expansions in surface-attached colonies of fluorescently-labeled microorganisms have contributed significantly to our understanding of fundamental evolutionary dynamics. However, experimental studies on genetic fluctuations in three-dimensional (3D) range expansions have been sparse, despite their importance for tumor or biofilm development. We encapsulated populations of two fluorescent *Escherichia coli* strains in inoculation droplets of volumes of only ~ 0.1 nl. The confined ensemble of cells grew when embedded in a hydrogel – with nutrients – and developed 3D colonies with well-defined, sector-like regions. Using a confocal laser scanning microscope (CLSM), we imaged the development of these 3D colonies and the emergence of sectors. We characterized how cell concentration in the inoculation droplet controls sector counts, growth rate, and the transition from branched colonies to quasi-spherical colonies. We further observed that the number of sectors on the surface tends to increase over time in contrast to what is known for 2D circular range expansions. The observation is consistent with the Eden growth model of two populations in 3D spherical growth. Ergo, our results demonstrate qualitative differences between 2D and 3D range expansions and their importance in gene fixation processes.

SIGNIFICANCE STATEMENT

Bacterial populations often form dense 3D colonies that provide various communal benefits. At the same time within the community, growth and competition for the goods and space causes strong segregation of sub-populations upon range expansion. We here provide a 3D version of the competition assay in a growing colony where we follow the demixing of two sub-populations using microscopy. We unravel how growth and competition control spatio-genetic patterning. We also confirmed the fragmentation of the subpopulations in expanding surface in addition to segregation, signifying the crucial difference between fixation processes in 2D and 3D range expansions.

INTRODUCTION

In nature, bacteria and other single cellular organisms live in communities and often form dense structured populations such as colonies or biofilms. The structure, function, and stability of these communities depend on a complex network of social interactions, where bacteria exchange signals and metabolites, and protect each other from toxins, while at the same time proliferating and competing for space. This continuous cooperation and competition in the communities lead to complex spatial structures.

The structure has been widely investigated in surface-colonizing microbial populations (see Ref. Eigentler et al. 2022a for a thorough review). These so-called *competition experiments*, in which well-mixed populations of bacteria (or yeast) Hallatschek and Nelson 2010 are inoculated on agar-surfaces and incubated, allow the cells to grow and divide and ultimately form complex macroscopic patterns Branda et al. 2005. When the initial founder cells are a mixture of differently colored fluorescent cells, one can observe patterns of spatially segregated lineages, even among bacteria of similar (i.e. neutral) fitness. It is well-known that the emergence of these sector-like regions is driven by random fluctuations at the outermost band of the expanding frontier Hallatschek et al. 2007. Also that the sector boundaries are diffusive Hallatschek and Nelson 2010, Korolev et al. 2011 and depend on, e.g., environmental conditions Excoffier and Ray 2008, Jauffred et al. 2017, extracellular matrix production Booth and Rice 2020, and cell shape Smith et al. 2017. Furthermore, the initial inoculating concentration has been found to control

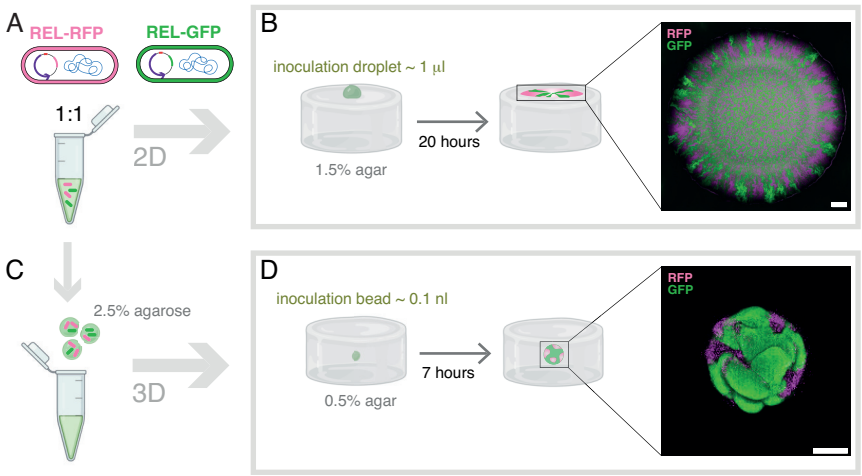

Figure 1: Competition experiments in 2D and 3D. **A:** 1:1 mixture of fluorescent *E.coli* REL coding for either GFP or RFP with concentration c_0 or multitudes of c_0. **B:** Sketch of competition experiment in 2D: Inoculation of an 0.5 μl inoculation droplet on M63+glu agar (1.5%) plate, followed by 20 hours of incubation (37°C). The inset is a (maximum intensity) z-projection of an example colony imaged by CLSM. The scale bar corresponds to 50 μm. **C:** Inoculation beads: Small agarose (2.5%) beads encompassing the 1:1 cell mixture from (A). **D:** Sketch of competition experiment in 3D: Inoculation of a 0.1 nl inoculation bead inside a M63+glu agar (0.5%), followed by 7 hours of incubation (37°C). The inset is a (maximum intensity) z-projection of an example colony imaged by CLSM. The scale bar corresponds to 50 μm. Elements of this figure were created with BioRender.com.

segregation patterns. In particular, the average sector regions' sizes correlate with inoculation density van Gestel et al. 2014, Blanchard and Lu 2015, Borenstein et al. 2015, Bottery et al. 2019, Lee et al. 2022, as space limits proliferation during range expansion Eigentler et al. 2022b. These observations provide us with a deeper understanding of the population structure in biofilm and also serve as the foundation to understand the genetic drift and fixation in expanding populations in 2D Hallatschek et al. 2007, Korolev et al. 2010, Fusco et al. 2016.

Bacteria also live in 3D habitats, often in dense environments, where they are mired in mucus or entangled in polymers secreted by other bacteria, algae, or animal tissue. One model system of bacteria living in such settings is monoclonal spherical colonies in hydrogel Jung et al. 2015. The system has been used to investigate, e.g., growth Strathmann et al. 2000, Burmølle et al. 2009, colony morphology Zhang et al. 2021, Cordero et al. 2022, quorum sensing Müller et al. 2022, and phage sensitivity Eriksen et al. 2018.

Despite these advances in 3D model systems and the broad interest in competition and evolution in microbial communities as well as tumor growth Fusco et al. 2016, Ben-Jacob et al. 2012, we still lack a suitable experimental model system to study competition in growing 3D bacterial colonies. Here, we propose such a system: We used a 1:1 co-culture of two fluorescently labeled *E. coli* strains, which we encapsulated in agarose beads. We submerged these *inoculation beads* in a semi-solid agar (0.5%) and incubated them for a 3D competition assay. We imaged the resulting colonies using a confocal laser-scanning microscope (CLSM), to know how the density of founder cells impacts growth and pattern-formation. We further analyzed how the number of sectors on the colony surface changes with time. Our findings are complemented with mathematical modeling to provide insight into spatial segregation in 3D communities. In particular, we demonstrate that the sector splitting, which we also observe in our experiment, becomes dominant in the long term. Our system serves as an effective tool to investigate the multi-species bacterial community and also as an ideal model system to analyze spatial population genetics in 3D growing colonies.

RESULTS

We mixed two sub-populations of an *E. coli* B strain (REL) carrying plasmids coding for either green fluorescent protein (GFP) or red fluorescent protein (RFP) in 1:1 ratio, as shown in Figure 1A. We verified that the cost of fluorescence-coding plasmid (i.e. growth rate) was indistinguishable for the two sub-strains: The generation times in the exponential growth phase in an M63 minimal medium supplemented with glucose (M63+glu) were (61±1) min and (57±1) min for the GFP and RFP carrying sub-strains, respectively (Supplementary Figure S1).

When a mixture of bacteria is inoculated on an agar surface, the population expands and segregates into monoclonal sectors.

Figure 1B is a sketch of such a (pseudo-)2D competition assay, where 0.5 μl droplets of the 1:1 mix were inoculated on agar (1.5%) supplemented with nutrients. In line with prior findings (Hallatschek et al. 2007), the expansion led to strong de-mixing of the two strains (inset of Figure 1B). In order to set up a 3D version of this experiment, we designed multi-cell beads based on a protocol by Roelof van der Meer and co-workers Buffi et al. 2011. This method, which is sketched in Figure 1C, relies on the hydrophobic nature of silicone oil to form small droplets of aqueous solutions. In our case, this solution is a mixture of bacteria and melted agarose (2.5%). We used this strategy to encapsulate the *E. coli* mixture (Figure 1A) in *inoculation beads*. When embedded in a semi-soft (0.5%) agar supplemented with nutrients and incubated (37°C), colonies outgrow the original agarose sphere to form 3D bacterial colonies as sketched in Figure 1D. The inset is an example of a colony derived from an inoculation bead with 1:1 mixture of fluorescent bacteria of concentration c_0, which corresponds to ~100 bacteria at the onset of the colony (Table 1).

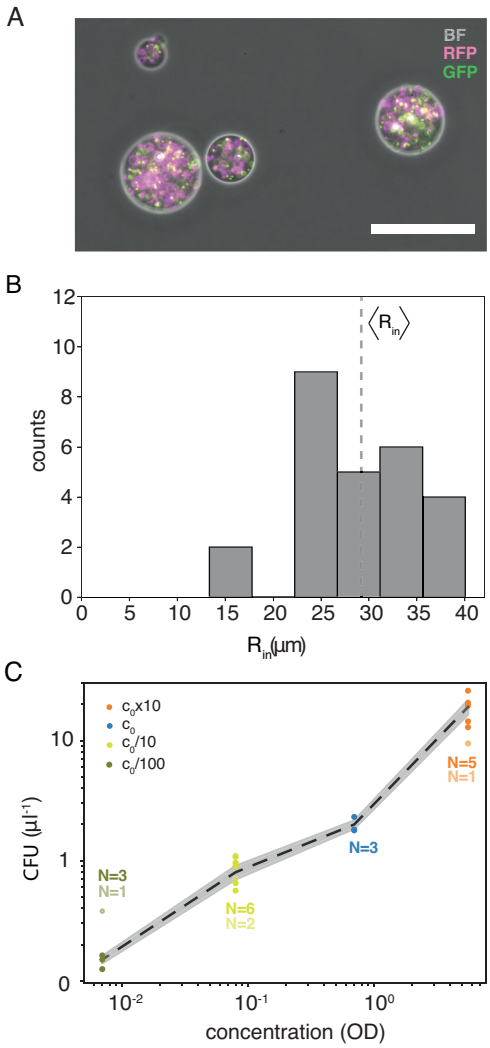

Figure 2: Inoculation bead characterization. **A:** Inoculation beads with c_0 concentration (Table 1). The image is an overlay of channels: bright-field (BF), green (GFP), and red (RFP). The scale bar is 100 μm. **B:** Distribution of inoculation beads' radii, R_{in}, with the average value (vertical dotted line): $\langle R_{in} \rangle = (29 \pm 7)$ μm (mean±SD, $N = 26$) as given in Eq. 1. **C:** Colony-forming inoculation beads (CFU) pr. volume versus density of founder cells, i.e., OD: $c_0/100$, $c_0/10$, c_0, and $c_0 \times 10$ on a double-logarithmic scale. Beads are either from frozen stocks (full color) or fresh from production (opaque), the latter is not included in the mean (punctuated line) and the shaded area corresponds to ±SEM.

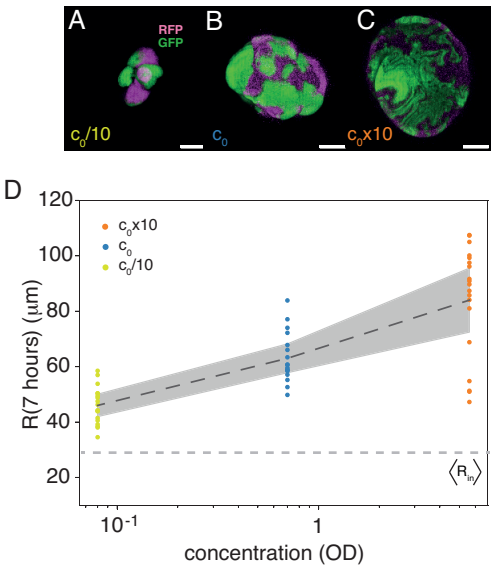

Figure 3: Density of founder cells controls size and patterning. **A-C:** Examples of colonies formed from inoculation beads with different initial concentrations of founder cells: $c_0/10$ (A), c_0 (B), and $c_0 \times 10$ (C). The scale bars correspond to 50 μm. **D:** Colony radii, $R(t)$, at $t = 7$ hours for $c_0/10$ (N=18), c_0 (N=17), and $c_0 \times 10$ (N=19). The punctuated line (dark gray) is the ensemble average (Eq. 1) and the shaded region corresponds to ±SEM. The horizontal punctuated line (light gray) is the average bead size, $\langle R_{in} \rangle$ (Figure 2B).

Inoculation bead characterization

Using wide-field fluorescence microscopy, we found that the spherical inoculation beads contain bacteria of both colors, as seen in Figure 2A. We found no bacteria outside the beads, implying that the agarose scaffold protects the cells from the toxic silicone oil (Supplementary Figure S2). Furthermore, we found that their radii, R_{in}, were distributed as given in Figure 2B, with average $\langle R_{in} \rangle = (29 \pm 7)$ μm (mean±SD, $N = 26$), which corresponds to a volume of about 0.1 nl. Hence, the inoculation volume is on the order of 10^3 times less than in the 2D case (0.5 μl). Our different batches of inoculation beads contained a 1:1 mix of the two colors (GFP and RFP) of bacteria and varying concentrations of cells: $c_0 \times 10$, c_0, $c_0/10$, and $c_0/100$ (Table 1). In order to estimate the concentration of beads that are able to grow into colonies, we plated the beads on a hard agar surface, incubated the plates, and counted the number of colony-forming units (CFUs). Figure 2C combines the counts fresh from production (opaque) and from frozen stocks (full color). Surprisingly, the concentration of beads with viable cells seemed to be increasing significantly with the initial cell concentration. This difference is much larger than the expected number of beads without cells based on Poisson statistics given our estimate of the number of bacteria in each bead (Table 1), see the Discussion section for further considerations. However, in practice we tuned the bead solution to have approximately the same amount of growing colonies pr. culture well.

Density of founder cells controls size and patterning

Following agar-embedment and incubation, we imaged colonies using a CLSM. We noted how often we found monocolor colonies (Supplementary Figure S3) but only imaged two-colored colonies. Figure 3A-C shows three examples of colonies grown from different batches of inoculating beads, i.e., $c_0/10$ (A), c_0 (B), and $c_0 \times 10$ (C) and incubated for 7 hours (37°C). At first sight, we found that not only does the size of the colony change with concentration, but also the patterning (more examples in Supplementary Figure S4). For a thorough analysis of this general observation, we segmented and filtered the 3D images to obtain a mask – with the thickness of a single voxel – reconstituting a connected surface and where all voxels were assigned one (and only one) color, see the insets of Figures 4-5 and Supplementary Movie 1 for examples. From this mask we estimated the time-dependent radius, $R(t)$ for $t = 7$ hours, of the projected surface (assuming spherical symmetry). In line with the general observation, $R(t)$ grows with the density of founder cells, as shown in Figure 3D.

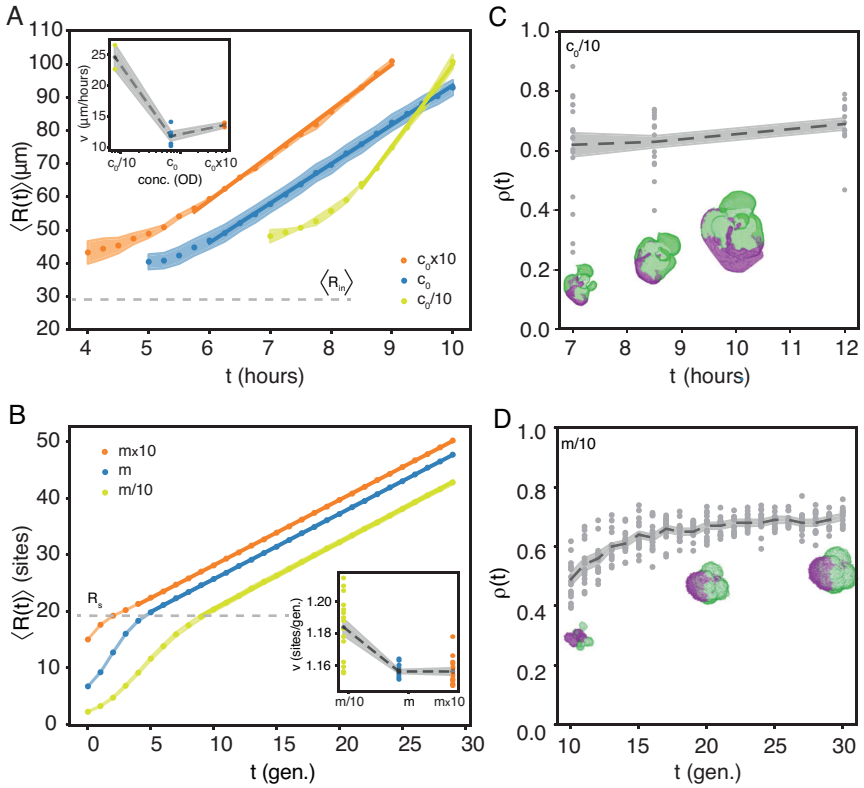

Figure 4: Density of founder cells controls growth dynamics. **A:** Ensemble-averaged colony radii, $\langle R(t)\rangle$, versus time (Eq. 1) for $c_0/10$ ($N = 2$), c_0 ($N = 5$), and $c_0 \times 10$ ($N = 2$). The full line is a linear fit and the shaded area signify ±SEM. The punctuated line is the mean radius of the inoculation beads, $\langle R_{in}\rangle$, found from Figure 2B. Inset: Radial growth speeds, v, of the individual traces versus concentration. The punctuated line is the the linear fits of the (full lines) and the shaded area signifies ±SEM. The dots are the slopes of the individual time-lapses. **B:** Ensemble-averaged *in silico* colony radii, $\langle R(t)\rangle$, versus time (Eq. 1) for $m/10$ ($N = 15$), m ($N = 15$), and $m \times 10$ ($N = 15$). The full line is a linear fit and the shaded area signifies ±SEM. The punctuated line is the mean radius, R_s, of the initial seeding sphere (i.e., inoculation beads). Inset: Radial growth speeds, v, of the individual traces versus concentration. The punctuated line is the the linear fits of the (full lines) and the shaded area signifies ±SEM. The dots are the slopes of the individual time-lapses. **C:** Isoperimetric quotient, $\rho(t)$ (Eq. 2), for different $c_0/10$ colonies at different times points, t: 7 hours ($N = 18$), 8.5 hours ($N = 16$), and 12 hours ($N = 12$). The punctuated line is the mean and the shaded area signifies ±SEM. The insets are the masks, M, from a time-trace(A), i.e., individual time points (yellow). **D:** Isoperimetric quotient, $\rho(t)$, for growing *in silico* colonies (N=15) of concentration $m/10$ over time, t. The punctuated line is the mean and the shaded area signifies ±SEM. The insets are examples from one model evaluation.

Density of founder cells controls growth dynamics

To study the dynamics of the 3D bacterial colony formation, we did time-lapses (Supplementary Movie 2) and Figure 4A shows the average radii, $\langle R(t)\rangle$, for the three concentrations: $c_0/10$ (yellow), c_0 (blue), and $c_0 \times 10$ (orange) as defined by Eq. 1. The time point at which we began imaging was chosen such that we easily found the small colonies under the microscope ($R > 40$ μm). Generally, we find an initial growth phase, where the colony radius expands slower than linear over time. This is followed by a temporal window, where $\langle R\rangle$ grows linearly over time (full lines) with the rate, v, given in the inset of Figure 4A. This linear expansion indicates that the colonies grow predominantly from the outermost cell layers due to insufficient nutrient penetration deeper in the colony Kuennen and Wang 2008. Also, this is well in accordance with earlier predictions Shao et al. 2017, Lavrentovich and Nelson 2015 and experimental findings for a similar *E. coli* system Cordero et al. 2022. Notably, from these earlier predictions, we would expect v to be similar for all concentrations, as is the case for c_0 and $c_0 \times 10$. However, our results from the lowest density of founder cells ($c_0/10$) contradict this view (inset of Figure 4A). Instead, the radial range expansion rate is significantly faster ($v \sim 25$ μm/hour vs. ~ 13 μm/hour). Assuming the doubling time to be ~ 1 hour (also inside 0.5% agar) and the volume of a single cell to be ~ 1 μm^3, this corresponds to a growing layer of the thickness of about 25 cells/hour.

As it is unclear how fewer inoculating cells result in faster radial growth, we explored this question employing a lattice model (Eden growth model) initiated from two kinds of seeds/cells with identical properties randomly placed in a sphere of radius, R_s, of three different concentrations: $m/10$, m, and $m \times 10$ (Materials and Methods). These seeds were allowed to divide into empty unoccupied neighboring sites until they eventually grow as one cluster Jullien and Botet 1985. The resulting pattern mimicked the competition of two populations in confined bacterial colonies. To study the dynamics of the resulting *in silico* colony formation (Supplementary Figure S5), we created time-lapse movies of growing colonies with different seeding concentrations (Supplementary Movie 3-5). Figure 4B shows the average radii, $\langle R(t)\rangle$, for the three concentrations: $m/10$ (yellow), m (blue), and $m \times 10$ (orange) in the linear growth part of the curve as defined by Eq. 1. In contrast to the experimental observation, we observed the initial growth ($\langle R(t)\rangle < R_s$) in the simulation to be faster, which settles to linear growth with a constant rate (inset of Figure 4B). We find large variations in v, especially for lowest seeding concentration ($m/10$). Moreover, the radial velocity is largest for this concentration, even though the difference is quite small.

In the Eden growth model, the expansion speed is dominated by the number of cells on the surface, i.e., cells neighboring empty lattice sites. Because colony shapes are rougher for lower concentrations of founder cells and for earlier times (Figure 4D), the radial growth at earlier times will be faster. Especially, when the colony is smaller than the seeding sphere ($\langle R(t)\rangle \leq R_s$) and the occupied lattice sites are not yet fully connected. Moreover, the colony morphologies could also cause fast growth of the colonies initiated from $c_0/10$ inoculation beads in the experiment. In particular, the protrusions on the surface enlarge the surface-to-volume ratio and may enhance growth by making nutrients accessible to a larger number of cells. To investigate this, we measured the time-dependent isoperimetric quotient, $\rho(t)$ (Eq. 2), for the projection of $c_0/10$ colonies, as shown in Figure 4C. $\rho(t)$ is a dimensionless measure of compactness and approaches its maximum 1 for a perfect circle projection. We found large scattering in $\rho(t)$, especially for small t, but the average $\rho(t)$ tends to grow slightly, as the cracks and valleys are filled and colonies become more round. For comparison, in Figure 4D, we measured $\rho(t)$ for the lowest concentration of the modeled data ($m/10$) for $t \geq 10$ generation time, when the colony is one connected structure and $\langle R(t)\rangle$ shows linear behavior over time (Figure 4B). We find the increase of average $\rho(t)$ over time converging to the value comparable to the experimentally observed $\rho(t)$.

Occupancy on colony surfaces matches the initial ratio in the inoculation bead

In order to evaluate any competitive advantage for one sub-population over the other, we measured the occupancy, O(7 hours), or the fraction of the GFP-expressing sub-strain on the colony surface (Eq. 3). We found equal occupancy of two sub-populations, as the fraction of the surface occupied by GFP-carrying cells is centered around $O = 1/2$ for all inoculation bead concentrations (Supplementary Figure S6). As the sub-populations have equal fitness advantage (Supplementary Figure S1), the final surface ratio corresponds to the 1:1 mixture in the inoculation bead. Also, we find from our model that time-dependent fluctuations in $O(t)$ are more important for smaller inoculation concentrations (Supplementary Figure S7).

Sector patterns are dynamic

We identified the different sectors on the colony surface and calculated their time-dependent areas, $A_{sec}(t)$, as given by Eq. 4. The distributions of $A_{sec}(t)$'s are shown in Figure 5A for both $c_0/10$ and c_0-derived colonies. We left the $c_0 \times 10$ out of the analysis, as the sectors were difficult to distinguish with our resolution. In both cases, small sectors are dominating in numbers, but a few large sectors occupy most of the surface area. Since the c_0-derived colony is bigger, naturally it has more of lager sectors as well as higher number of sectors.

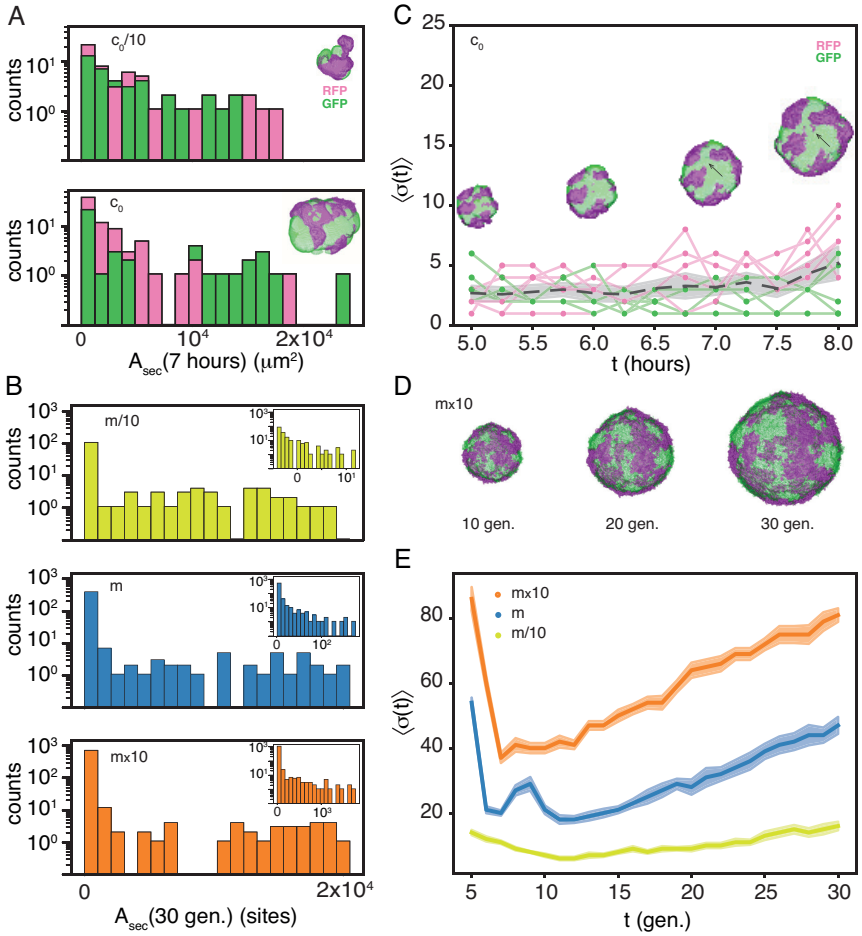

Figure 5: Sector patterns are dynamic. **A:** Distributions of areas of sectors of sub-population on the experimental colonies' surfaces, $A_{sec}(t)$, at $t = 7$ hours for $c_0/10$ RFP ($N = 52$) and GFP ($N = 40$) sectors, as well as c_0 RFP ($N = 76$) and GFP ($N = 47$) sectors. The insets are surface masks, M, for the given concentration. **B:** Distributions of areas of sectors of sub-population on the *in silico* colonies' surfaces, $A_{sec}(t)$, at $t = 30$ generations for $m/10$ ($N = 233$), m ($N = 702$), $m \times 10$ ($N = 1219$). Insets: The insets are the same distributions but within a smaller range and the same number of bins (20). **C:** Ensemble-averaged number of sectors, $\langle\sigma(t)\rangle$, versus time, t, (punctuated line) as given in Eq. 4 for c_0 ($N = 5$). The dots are the number of sectors for RFP (magenta) and GFP (green) individually. The shaded area signifies ±SEM. Inset: The time evolvement of surface sectors for a c_0-derived example colony. An example of sector splitting is designated (black arrows). **D:** An example of how surface sectors changes with time, $t \in \{10, 20, 30\}$ generations in a $m \times 10$-derived modeled colony. **E:** Ensemble-averaged number of sectors, $\langle\sigma(t)\rangle$, versus time, t, (Eq. 4) for concentration: $m/10$ (yellow), m (blue), and $m \times 10$ (orange) as given in Eq. 4. There is no distinction between the two-colors of sectors and the number of colonies is ($N = 15$). The shaded area signifies ±SEM.

These results were paralleled in our models for $m/10$, m, and $m \times 10$ in Figure 5B. We found that sectors with lower $A_{sec}(t)$ for $t = 30$ generations are most frequent for our seeding concentrations (see also the inset for the frequency of small sectors in higher resolution), but the total number of sectors is less for that lower seeding concentration.

We finally looked into how the number of sectors changes with time, $\sigma(t)$, for REL+RFP (magenta) and REL+GFP (green) in c_0-derived colonies in Figure 5C. Based on the time-lapses of 5 colonies, we found that the ensemble-average, $\langle\sigma(t)\rangle$, as defined in Eq. 4, goes up within our time range. This corresponds to a splitting of sectors, as shown for one example in the inset of 5C (black arrow). As we know that we miss the smallest sectors with the resolution of our system, we set out to investigate this further using our Eden growth model. Example colony at different t is shown in Figure 5D. As shown in Figure 5E, the average $\langle\sigma(t)\rangle$ decreases at the early time dominated by the merging of clusters from different founder cells (note that we counted spatially separated clusters as different sectors), but after the clusters are connected the cells start to grow as one colony, hereafter sector splitting dominates and gives an increase in $\langle\sigma(t)\rangle$.

DISCUSSION

Recent advances in 3D culture technology allow for *in vitro* models of development and disease with organoids (i.e., simplified organs) Bredenoord et al. 2017 or tumorospheresWeiswald et al. 2015, Costa et al. 2016, respectively. The counterpart of these 3D models within bacteriology research is quasi-spherical colonies, grown from a few bacteria embedded in agar. We propose 3D cultures initiated from agarose droplets could be this simple (yet highly controllable) multi-species model of biofilm-formation in soil, natural water environments, minerals or other substrates.

In the present manuscript, we presented a method, which in brief, substitutes the inoculation droplet with an inoculation bead of much smaller volume (fractions of μl versus nl). So, our colonies are initiated from very small volumes and we can, hence, inquire about the early stages of colony development. Furthermore, we interchanged the hard agar (> 1%) substrate with submersion in soft agar (< 1%), which allows for studies of spherical range expansion. We used confocal laser-scanning microscopy (CLSM) for imaging but other techniques to optimize the resolution and light penetration in large cell agglomerates are evolving rapidly (e.g light-sheet microscopy Tomer et al. 2012). Even though advanced imaging is required for proper 3D reconstitution, we anticipate that many questions could be answered by 3D competition assays under wide-field fluorescence microscopes.

Unexpectedly, we found that the concentrations of viable beads increased with the density of founder cells (Figure 2C). Possible explanations could be that i) more beads were formed per volume when the cell density is higher, possibly cells acting as nucleation centers for large droplets ii) not all cells were encapsulated in the beads and hence the empty beads fraction was higher than expected, iii) a fraction of encapsulated cells are not viable, and/or iv) only the bacteria closest to the inoculation bead's surface can grow and form a visible colony.

From 2D competition experiments we know that sector boundaries are diffusive Hallatschek et al. 2007 and for polar cells even super-diffusive Hallatschek and Nelson 2010. The reason for this is that uni-axial growth of rod-shaped bacteria (i.e. *E. coli*) results in chain-formation of bacteria. As compressing forces make small asymmetries in cell alignment, these instabilities propagate to cause jagged shapes on surface-attached monolayers Boyer et al. 2011, Rudge et al. 2013. These shapes are further enhanced by inter-cellular adhesion, which leads to increased diffusivity of mixing and area of interaction between lineages Kan et al. 2018. We find similar patterns of jagged sector boundaries on the colonies' surfaces (Figure 3C), even though our boundaries are 2D interfaces between sectors. This highlights an interesting following-up question: how does cell alignment affect the spatio-temporal dynamics of sectors?

The Eden growth model predicts a transition from super-linear growth in early colonies to slower (i.e. linear) surface expansion over time (Figure 4B). The super-linear regime largely overlaps with the regime where the growth – starting from the individual founder cells – is not yet connected into one colony. Our experimental resolution did not allow us to observe such early super-linear dynamics, but we observed the linear surface expansion in experiments. The reason for this linear regime is that behind the fast-growing surface cells, is a quiescent region, where proliferation is slower because of space constraints Tuson et al. 2012 and metabolite diffusion from the colony periphery Shao et al. 2017, Lavrentovich and Nelson 2015, Lavrentovich et al. 2013a. We also find that the entrance into the linear regime depends on the initial concentration of founder cells, where the colonies with highest initial concentration reaches this compact-mature colony state earlier (Figure 4A). This is also consistent with the simulations (Figure 4B).

We also found that, for the lowest density of founder cells, the colonies have a rougher surface growth as earlier reported Martínez-Calvo et al. 2022. The cells located in these bumps or protuberances are expected to have better availability of nutrients, which can be part of the explanation for their observed faster radial growth (inset Figure 4A). The model also showed slightly faster growth for lower initial cell density (inset Figure 4B), though the difference was small. Furthermore, we found that the surface roughness decreases slowly with time and the colonies become rounder and rounder (Figure 4C). For 2D colony growth, it has been established that colony morphology qualitatively changes with nutrient availability and agar hardness.

Specifically, nutrient-poor environment and/or harder agar can cause instabilities to develop branching Ohgiwari et al. 1992. Similar instabilities are expected in 3D growth under certain environmental conditions. The observed lack of strong instabilities in our system supports the use of the Eden growth model that ignores inhomogeneity and nutrient depletion of the environment. However, to understand the growth dynamics quantitatively, a model that considers these factors would be desirable.

We have demonstrated that the sectors on the surface can merge but also split over time. In our experiments, we observed the splitting events, and the number of sectors showed a tendency to increase, though fluctuation was large (Figure 5C). These observations are consistent with the two-species Eden growth model simulation. In 3D expanding colonies, individual clusters – starting from individual seeds – quickly merge to form a connected colony, and after that, although large sectors do form, they also fragment forming small sectors. Therefore, the number of sectors actually increases over time (Figure 5E). This contrast what we know from 2D radial expansions, where an initial coarsening phase, in which domain boundaries annihilate, is followed by a stable phase, in which the number of sectors does not change Hallatschek et al. 2007. This behavior in the 2D system is the consequence of initial merging of sectors, due to the diffusion of sector boundaries and the expansion of the radial frontier, which is inflating the sector boundary. This results in the crossover time $t^* \sim R_0/v$ after which the coarsening is suppressed Lavrentovich et al. 2013b. Here, R_0 is the radius of the initial "homeland" which determines the length scale of the initial sectors, and v is the expansion speed of the radius. In 3D, the sector boundary on the surface is a fluctuating line. When we ignore the effect of the roughness of the surface, the surface dynamics of the two-species Eden growth model are expected to show the same dynamics as the voter model Lavrentovich and Nelson 2015, Lavrentovich et al. 2013b. For the voter model on a flat surface, the coarsening dynamics over time t is marginal, where the density of the boundary between the sectors decreases in proportional to $1/\ln t$. Because there is no "surface tension" to keep the sector boundaries compact, an initially smooth sector boundary tends to fragment into small sectors, slowing down the coarsening significantly Dornic et al. 2001. In the spherical expansion, the increase of the surface area is expected to suppress the already marginal coarsening. It should be noted, however, that the total surface area is increasing proportional to t^2. The number of sectors per area in the Eden growth model showed a decreasing tendency over simulated time especially for the high-seed concentration (Supplementary Figure S11). This suggests that the expansion of existing sectors dominates most of the surface. In addition, it is worth noting that the roughness of the surface can affect the coarsening dynamics Kuhr et al. 2011. A further theoretical study is needed to characterize mixing and demixing dynamics in 3D range expansion quantitatively.

As our method is both cheap and easy to set up, this can be a natural extension of the original 2D competition assay to study 3D dynamics. The method can also provide a platform for a broad range of investigations with the potential for high throughput experiments Friedrich et al. 2009. Furthermore, this model system could be used to resolve, not only how bacterial competition drives spatio-genetic patterning in neutral competition, but also how selective advantage, competitive interaction, cooperation, and division-of-labor among the different cells distort this pattern in 3D growth by introducing different interacting cell types Lee et al. 2022, Dal Co et al. 2020, Borer et al. 2020, Celik Ozgen et al. 2018. Therefore, we anticipate that the proposed accessible method can help advance our understanding of microbial community development and evolution in related systems in 3D environments significantly.

MATERIALS AND METHODS

Bacterial strains and culture media

We used two sub-populations of the *Escherichia coli* B strain REL606 Monds et al. 2014 carrying plasmids that constitutively expressed kanamycin resistence and either green fluorescent protein (GFP), pmaxGFP (pmaxCloning-Vector, Lonza), with excitation/emission 487/509 nm or red fluorescent protein (RFP), pTurboRFP (pmaxCloning-Vector, Lonza), with 553/574 nm Smith et al. 2017. Therefore all media used in this study was supplemented with 30 μg/ml kanamycin to retain fluorescence.

Through this study we alternated between the following two medias: the rich Lysogenic broth (LB) with 1% Bactotryptone, 0.5% NaCl, and 0.5% yeast extract and the M63 minimal media (M63+glu) with 20% 5×M63 salt Elbing and Brent 2002, 1 μg/ml B1, 2 mM $MgSO_4$ and 20 μg/ml (w/v) glucose.

Encapsulating bacteria in inoculation beads

For a 3D competition experiment, we produced 2.5% agarose beads following the procedure of Ref. Buffi et al. 2011. One day prior to bead-formation, pipette tips were placed in an incubator set to 60°C, two overnight cultures of REL+GFP and REL+RFP in 2 ml of LB were prepared, and incubated at 37°C under constant shaking. The following day, we measured (NanoPhotometer C40) the optical densities at the wavelength of 600 nm (OD) of the overnight cultures. Then, we prepared a saturated 1:1 mixture, by mixing the overnight cultures in the ratio corresponding to their ratio of the measured ODs. Meanwhile, 15 ml of silicone oil (dime-thylpolysiloxane, Sigma) in a 50 ml tube was heated in a block heater at 55°C (AccuBlock Digital Dry Baths, Labnet International, Inc.) for ~ 20 min. Then, sterile 2.5% agarose (VWR Life Science, EC no:232-731-8, CAS

	[OD]	[cells/ml]	[cells/bead]
$c_0/100$	$6.9 \cdot 10^{-3}$	$1.6 \cdot 10^{7}$	1.0±0.7
$c_0/10$	$8.2 \cdot 10^{-2}$	$1.21 \cdot 10^{8}$	12±9
c_0	0.70	$1.06 \cdot 10^{9}$	108±78
$c_0 \times 10$	5.6	$8.46 \cdot 10^{9}$	863±625

Table 1: Inoculating bead's concentration in units of OD or cells/ml, using the conversion OD= 1 equal to $1.5 \cdot 10^9$ cells/ml. The 4th column is the calculated number of cells/bead, using the average volume: $\frac{4}{3}\pi\langle R_{in}\rangle^3$ (Figure 2B) and the error correspond to ±SD propagated from the $\langle R_{in}\rangle$ error.

No:9012-36-6) in Mili-Q water was melted in a microwave. We made sure to i) shake rigorously for homogeneity and ii) avoid boiling to minimize evaporation. Then, the agarose solution was left to cool to ~55°C, before 500 μl was transferred to a 2 ml (heated) tube in the block heater (55°C). Afterwards, 15 μl of pluronic acid (Pluronic F-68 solution 10% Sigma) was added and the tube was transferred to a shaker block heater (Thermometer Confort, Eppendorf) set at 42°C. After few minutes, 2-100 μl of the saturated 1:1 bacteria culture was added under continuous vortexing (1400 rpm) for final concentrations of OD $\in \{5.6, 0.70, 8.2 \cdot 10^{-2}, 6.9 \cdot 10^{-3}\}$ (Table 1). We removed the silicone oil from the block heater and – using the pre-heated pipette tips – 500 μl of this bacteria-agarose-pluronic acid mix was added drop by drop to the silicone oil. This step was done fast to avoid untimely solidification of the agarose (at temperatures < 25°C). Afterwards, the 50 ml tube containing the droplets in silicone oil was vortexed (Vortex Mixer, Labnet International) for 2 min at maximum speed before being placed in a water-ice bath for additional 10 min. Then, centrifuged for 10 min at 500 g (room temperature), before the silicone oil was removed by careful pipetting followed by 2× washing: i) Addition of 5 ml of phosphate buffered saline (PBS), ii) centrifugation for 10 min at 500 g, and iii) gentle removal of oil and supernatant. Finally, the washed beads were resuspended (by vortexing) in 5 ml of PBS.

To harvest the beads, we let bead-PBS solution flow through a set of strainers with mesh sizes of 70 μm (Cell strainer 70 μm Nylon, BD Falcon) and 40 μm (Cell strainer 40 μm Nylon, BD Falcon), placed on a 50 ml tube. An additional 5 ml of PBS was poured through the strainers to ease the passage. To collect the selected beads, the 40 μm strainer was placed upside down on a new 50 ml sterile tube and the beads adsorped to the filter surface were desorbed by rinsing with 6 ml of LB medium. For long-term storage, the bead-medium solution was aliquoted in volumes of 500 μl in 2 ml vials, before mixing with 500 μl of 50% glycerol-solution (11 vials pr. batch), and stored at -80°C. We used 1 ml serological pipette tips for bead handling to prevent damaging flow rates.

Growth rate measurements

Cultures of REL+GFP and REL+RFP were incubated (37°C) in parallel overnight in 2 ml of M63+glu under constant shaking. The following day, 500 μl of each overnight culture were diluted in 5 ml of M63+glu and the ODs were measured over 5 hours with a sampling rate of ~ 30 minutes.

Inoculation bead concentration measurements

Ratio of colored strains To verify that the ratio in the beads (tuned with OD ratios), we serially diluted ($10^6\times$) the saturated 1:1 cell mixture (for encapsulation) and plated (50-200 μl) on LB plates with agar (1.5%). The plates were incubated overnight, and the number of CFUs from REL+RFP and REL+GFP was counted to verify the 1:1 ratio (Supplementary Figure S8).

Cells pr. bead Overnight cultures of REL+GFP and REL+RFP was serially diluted ($10^6\times$) and plated (50 μl) on LB plates with 1.5% agar. From the number of CFU, we found that OD= 1 corresponds to ~ $1.5 \cdot 10^9$ cells/ml. Combined with OD$\in \{5.6, 0.70, 8.2 \cdot 10^{-2}, 6.9 \cdot 10^{-3}\}$ and the average bead volume, we estimated the average number of cells pr. bead given in Table 1.

Beads pr. volume We mixed 80 μl of inoculation beads, either directly from production or from frozen vials, with 200 μl medium (LB). The mixture was plated by gently whirling (no spatula) on LB plates with 1.5% agar, then the plates were incubated overnight, and finally the number of CFUs was counted. This estimation of beads pr. volume was used to determine the proper dilution after thawing to ultimately get ~ 20 beads pr. well.

Imaging inoculation beads

To estimate inoculation beads' radii, beads were imaged with an inverted Nikon Eclipse Ti fluorescent microscope (Nikon, Tokyo, Japan) using a 20× air immersion objective (Splan flour,L20×,0.45corr∞) paired with an Andor Neo camera (Andor, Belfast, UK). GFP and RFP was excited by a Hg lamp using the FITC and Texas-red (Nikon, Tokyo, Japan) cubes, respectively.

Toxicity measurements

To evaluate the toxicity of silicone oil and pluronic acid, we did limiting dilution experiments: Overnight cultures of REL+GFP and REL+RFP was (10 - 10^7)× diluted in 1 ml of either pluronic acid, silicone oil, or PBS as control. Then the number of viable cells was determined by plating (LB plates with 1.5% agar) followed by CFU counting.

Competition assays

Embedment of inoculation beads in 0.5% agar In line with methods detailed in Cordero et al. 2022 and references therein, bottles of 20 ml milipore water with 0.625% agar were melted by repeated cycles of heating (in the microwave) and shaking to ensure homogeneity and minimize evaporation and aging Mao et al. 2017. After cooling (~55°C), we added M63 salt Elbing and Brent 2002 and supplements to a final M63+glu with 0.5% agar. Then, 1 ml of this solution was transferred to a pre-heated tube in the (non-shaking) block heater (55°C). A frozen vial of bead-medium solution was thawed (on the bench) for ~5 min until melted and 20-500 μl were transferred into 1 ml of LB (to minimize the time spend in high-concentration glycerol). Meanwhile, the agar-medium solution was supplemented with 10 μl of a 1 M stock of KNO_3 – to avoid growth difficulties in anoxic conditions as suggested by Refs. Sønderholm et al. 2017, Kvich et al. 2019 – and 30 μg/ml kanamycin. Quickly hereafter, 50 μl of the diluted bead-medium solution was added and the tube's content was mixed and poured into a glass bottomed culture well (WillCo HBST-5040). Here it was left to solidify for a few minutes on the bench before incubation (upside-down) at 37°C for at least 5 hours (see imaging section). The agar had a final thickness of ~ 300 μm and contained 17±5 inoculation beads/well (Supplementary Figure S9); corresponding to at the most one bead for every 50 μl agar. For 3D competition experiments, the wells were incubated at 37°C for 5-7 hours (depending on the experiment).

Deposition of inoculation droplets on 1.5% agar In line with the protocol of Ref. Jauffred et al. 2017 and references therein, we mixed 1:1 overnight cultures of REL+GFP and REL+RFP with LB to a final OD=0.7 before inoculating 0.5 μl on plates with M63+glu and 1.5% agar. Plates were incubated for 20 hours at 37°C.

Imaging competition assays

3D colony images After incubation, we checked all culture wells to discard those, where colonies had outgrown the agar and spread over the agar-air interface. All colonies of the remaining culture wells were imaged with CLSM (Leica SP5) and a 20× air objective (NplanL20×0.40NA). The data was acquired with sequential z-stacks of RFP (488 nm laser, detection range of (498-536) nm) followed by GFP (543 laser, detection range of (568-641) nm) to a final image of voxel size in (x,y,z) of (1.51,1.51,1.33) μm. For every new condition, we made sure to collect images from at least 2-3 different wells.

Time-lapse 3D images After 4-7 hours of incubation, our colonies had outgrown the inoculation beads and reached a diameter of ~ 100 μm. For CLSM time-lapses, our microscope was equipped with a standard water-based heating stage set to 37°C and we did 5 hours of imaging with a frame rate of 4/hour. We repeated this 2-5 times for each condition. We also investigated time-evolvement by comparing individual sets of colonies incubated for different amount of times. The visualization was made using the Fiji 3D viewer plugin Schmid et al. 2010.

2D colony images The agar plate was placed up-side down on our inverted CLSM. They were imaged with sequential z-stacks using a similar procedure as for the 3D colonies but with an 5× air objective (Nplan5×0.12PHO, Leica). The voxel size in (x,y,z) was (6.07,6.07,10.33) μm and we used Pairwise Stitching Preibisch et al. 2009 plugin for Fiji.

Image analysis

Segmentation of 3D colonies The 3D image segmentation was done using both BiofilmQ Hartmann et al. 2021, Matlab, and Fiji/Image J Schindelin et al. 2012 and the following work flow. First, the segmentation was done separately for each channel (GFP+RFP) in BiofilmQ. We cropped the image stacks in z-direction (same z for both channels) to discard the colony half-sphere furthest away from the objective, which was distorted by strong shadowing effects. Then, we de-noised the images

by convolution ([kernel size: [x,y,z] = [5,5,3] pixels) to soften the edges and fill the holes between cells. Using the Otsu method (with 2 classes: object and background), we manually selected the threshold value for each image in the stacks. Afterwards, we checked – using the Overlay function – that the segmentation matched the raw data. Hereafter, the resulting masks of the channels (GFP+RFP) were divided into small cubic volumes of length 1.52 μm, which reflects the voxel size of the image and corresponds 2-4 *E. coli* volumes. Hereafter, the channel masks were merged, and the surface of the resulting mask was found calling Cube_Surface followed by the Filter Objects function with Cube_Surface in the range [1,2]. The resulting segmentation of the merged channels were saved (mat-file) and the Cube_Surface voxel indices vector was converted to a matrix (using Cell2mat). The matrix can be read as a 3D logical image of a connected surface, but what we wanted was a hollow half-sphere with the thickness of a single voxel. Therefore, we manually removed the surface furthest away from the objective using the Paintbrush tool in Fiji.

The resulting segmentation mask, was multiplied separately with each segmented channels (GFP and RFP) and then merged to the resulting surface mask. We found the number of voxels in the surface mask that was assigned both colors (GFP and RFP), to be (3 ± 2)%, (4 ± 1)% and (11 ± 4) % for $c_0/10$, c_0, and $c_0 \times 10$, respectively (Supplementary Figure S10). As they are few and that RFP in our system is less detectable, we decided to assign all these two-colored voxels to RFP. We also found that the surface mask had some discontinuities (<‰), using 3D Fill Holes plugin in Fiji Ollion et al. 2013. Hence, the resulting surface mask, M, is a single layer of voxels each with one and only one color (see an example in the Supplementary Movie 1).

Size estimation of 3D colonies From z-projections of the mask M (or the thresholded image of beads), we obtained logical (x,y)-images. The projected areas of the n-th colony (bead), $A^{(n)}_{prj}$, was found by counting pixels $\neq 0$ and multiplying by pixel area conversion in (x,y). By assuming the colony (bead) to be spherical, we estimated the ensemble-averaged radius, R, at time t to be:

$$\langle R(t) \rangle = \frac{1}{N\sqrt{\pi}} \sum_{n=1}^{N} \sqrt{A^{(n)}_{prj}(t)}, \tag{1}$$

where N is the total number of colonies.

Determining perimeter in 3D bacterial colonies From z-projections of the mask M (or the manual thresholded images of the z-projections), the projected perimeter, P, of the n-th colony was found by using the Fiji function called Analyze Particles.

Isoperimetric quotient Measuring the perimeter, P, of $A_{prj}(t)$ for a projection of a colony we found the ratio between $A_{prj}(t)$ and the area of a circle with the same P, called the isoperimetric quotient for a colony to be:

$$\rho(t) = 4\pi \frac{A_{prj}(t)}{P^2}, \tag{2}$$

which is a dimensionless measure of compactness with the maximum compactness for a perfect circle ($\rho = 1$).

Determining occupancy in 3D bacterial colonies We defined the ensemble-averaged occupancy of GFP-expressing bacteria, O, on the colony surface as the sum over the following ratio:

$$\langle O(t) \rangle = \frac{1}{N} \sum_{n=1}^{N} \frac{A^{(n)}_{GFP}(t)}{A^{(n)}(t)}, \tag{3}$$

where $A^{(n)}_{GFP}(t)$ is the area of GFP-expressing bacteria and $A^{(n)}(t)$ is the total surface area of the n-th colony at time t, such that $A^{(n)}(t) = A^{(n)}_{GFP}(t) + A^{(n)}_{RFP}(t)$.

Counting sectors in 3D bacterial colonies We defined 3D sectors as connected regions on the colony surface using the Fiji plugin Find Connected Regions on the colony mask M with a minimum sector area of 10 voxels (~23 μm^2). This value was chosen to be optimal for our dataset by comparing the automated sector counts, $\sigma(t)$, with manual counts. We counted the number of GFP and RFP sectors. We also found the ensemble-averaged number connected sectors (GFP+RFP) on the colony surface:

$$\langle \sigma(t) \rangle = \frac{1}{N} \sum_{n=1}^{N} \frac{1}{K} \sum_{k=1}^{K} A^{(n)}_{sec(k)}(t), \tag{4}$$

where $A^{(n)}_{sec(k)}(t)$ is the area on the colony mask of the k-th sector of GFP-expressing bacteria of the n-th colony at a given t. We calculated $A^{(n)}_{sec(k)}(t)$ by scaling the number of voxels in the sector with the conversion in (x,y).

For the modeled colonies we used the minimum sector area of 1 lattice site, as there is no ambiguity in the assignment of colors in this case.

Three dimensional Eden growth model

We employed 3D Eden growth model to simulate bacterial colonies grow from an inoculation bead in a 3D environment. The model divides the space into a cubic lattice, where each lattice site can be occupied by "bacteria" or empty, and the growth happens if there is an empty neighbor site. It should be noted that the correspondence of the length and time scale between the model and the experiment is only qualitative; this is a coarse-grained model where one occupied lattice site represents a meta-population of a cluster of several cells Fusco et al. 2016.

Initial condition In a 3D cubic-lattice of size $(L \times L \times L)$ with $L = 200$, we placed (in the center) a sphere of radius, $R_s = 19$ lattice sites. Individual seeds were placed randomly inside the sphere and the number of seeds were on average N $\in \{12, 108, 863\}$ drawn from a 1:1 distribution of the two colors of seeds (1 or 2), corresponding to seeding concentrations of $m/10$, m, and $m \times 10$. More specifically, we filled each site inside the sphere with the probability N/V with $V = \frac{4}{3}\pi R_s^3$, with one of the two colors assigned with equal probability.

Update rule We first make a list S containing all surface sites, i.e., occupied sites with one or more empty neighboring sites out of the 6 neighbors. The growth is done as follows: (i) Choose one site to divide from the sites in the list S randomly with equal probability. (ii) Randomly choose one of the empty neighbor sites of the chosen site in (i). (iii) Fill the chosen site in (ii) with the same color as the chosen site in (i). (iv) Update the list S such that a) the new site was added to S if it had one or more empty neighboring sites and b) the sites were removed from S if they no longer had any empty neighboring sites. We repeated (i)-(iv) $5 \cdot 10^5$ times. For every division, the time proceeds by the inverse of the number of surface sites in S, meaning that a unit of time corresponds to the "generation time" (an occupied site on the surface duplicates on average once per unit of time).

We coded the model in C++ using a C++ library Armadillo (Sanderson and Curtin 2016).

Statistics

All mean values are given as mean plus/minus the standard error of the mean (SEM) or the standard deviation (SD) and only when data are tested against the null hypothesis that it is normally distributed. For distributions, bin sizes were chosen following Sturge's rule, unless stated otherwise.

ACKNOWLEDGMENTS AND FUNDING SOURCES

The authors thank Martin Møller Larsen for fruitful discussions on the modeling and for providing parts of the code for the modeling. The authors also thank Thu Trang Nguyen for providing the conversion factor from optical density to number of cells (colony forming units) and Nathánaël van den Berg for assistance in the competition experiment in 2D.

This work was funded by Danmarks Frie Forskningsfond grant DFF0165-00032B and DFF0165-00103B (LJ) and by Novo Nordisk Fonden grant NNF21OC0068775 (NM).

REFERENCES

Eigentler, L., F. A. Davidson, and N. R. Stanley-Wall, 2022. Mechanisms driving spatial distribution of residents in colony biofilms: an interdisciplinary perspective. *Open Biology* 12:220194. https://royalsocietypublishing.org/doi/10.1098/rsob.220194.

Hallatschek, O., and D. R. Nelson, 2010. LIFE AT THE FRONT OF AN EXPANDING POPULATION. *Evolution* 64:193–206. https://academic.oup.com/evolut/article/64/1/193/6854125.

Branda, S. S., Ã. Vik, L. Friedman, and R. Kolter, 2005. Biofilms: the matrix revisited. *Trends in Microbiology* 13:20–26. https://linkinghub.elsevier.com/retrieve/pii/S0966842X04002604.

Hallatschek, O., P. Hersen, S. Ramanathan, and D. R. Nelson, 2007. Genetic drift at expanding frontiers promotes gene segregation. *Proceedings of the National Academy of Sciences* 104:19926–19930. https://pnas.org/doi/full/10.1073/pnas.0710150104.

Korolev, K. S., J. B. Xavier, D. R. Nelson, and K. R. Foster, 2011. A Quantitative Test of Population Genetics Using Spatiogenetic Patterns in Bacterial Colonies. *The American Naturalist* 178:538–552. https://www.journals.uchicago.edu/doi/10.1086/661897.

Excoffier, L., and N. Ray, 2008. Surfing during population expansions promotes genetic revolutions and structuration. *Trends in Ecology & Evolution* 23:347–351. https://linkinghub.elsevier.com/retrieve/pii/S0169534708001675.

Jauffred, L., R. Munk Vejborg, K. S. Korolev, S. Brown, and L. B. Oddershede, 2017. Chirality in microbial biofilms is mediated by close interactions between the cell surface and the substratum. *The ISME Journal* 11:1688–1701. https://www.nature.com/articles/ismej201719.

Booth, S. C., and S. A. Rice, 2020. Influence of interspecies interactions on the spatial organization of dual species bacterial communities. *Biofilm* 2:100035. https://linkinghub.elsevier.com/retrieve/pii/S2590207520300174.

Smith, W. P. J., Y. Davit, J. M. Osborne, W. D. Kim, K. R. Foster, and J. M. Pitt-Francis, 2017. Cell morphology drives spatial patterning in microbial communities. *Proceedings of the National Academy of Sciences* 114:E280–E286. http://www.pnas.org/lookup/doi/10.1073/pnas.1613007114.

van Gestel, J., F. J. Weissing, O. P. Kuipers, and A. T. Kovács, 2014. Density of founder cells affects spatial pattern formation and cooperation in \emph{Bacillus subtilis} biofilms. *The ISME journal* 8:2069âĂŞ2079. http://www.ncbi.nlm.nih.gov/pubmed/24694715.

Blanchard, A. E., and T. Lu, 2015. Bacterial social interactions drive the emergence of differential spatial colony structures. *BMC Systems Biology* 9:59. https://bmcsystbiol.biomedcentral.com/articles/10.1186/s12918-015-0188-5.

Borenstein, D. B., P. Ringel, M. Basler, and N. S. Wingreen, 2015. Established Microbial Colonies Can Survive Type VI Secretion Assault. *PLOS Computational Biology* 11:e1004520. https://dx.plos.org/10.1371/journal.pcbi.1004520.

Bottery, M. J., I. Passaris, C. Dytham, A. J. Wood, and M. W. van der Woude, 2019. Spatial Organization of Expanding Bacterial Colonies Is Affected by Contact-Dependent Growth Inhibition. *Current Biology* 29:3622–3634. https://linkinghub.elsevier.com/retrieve/pii/S0960982219311558.

Lee, H., J. Gore, and K. S. Korolev, 2022. Slow expanders invade by forming dented fronts in microbial colonies. *Proceedings of the National Academy of Sciences* 119:1–8. https://pnas.org/doi/full/10.1073/pnas.2108653119.

Eigentler, L., M. Kalamara, G. Ball, C. E. MacPhee, N. R. Stanley-Wall, and F. A. Davidson, 2022. Founder cell configuration drives competitive outcome within colony biofilms. *The ISME Journal* 16:1512–1522. https://www.nature.com/articles/s41396-022-01198-8.

Korolev, K. S., M. Avlund, O. Hallatschek, and D. R. Nelson, 2010. Genetic demixing and evolution in linear stepping stone models. *Reviews of Modern Physics* 82:1691–1718. https://link.aps.org/doi/10.1103/RevModPhys.82.1691.

Fusco, D., M. Gralka, J. Kayser, A. Anderson, and O. Hallatschek, 2016. Excess of mutational jackpot events in expanding populations revealed by spatial LuriaâĂŞDelbrück experiments. *Nature Communications* 7:12760. https://www.nature.com/articles/ncomms12760.

Jung, Y.-G., J. Choi, S.-K. Kim, J.-H. Lee, and S. Kwon, 2015. Embedded Biofilm, a New Biofilm Model Based on the Embedded Growth of Bacteria. *Applied and Environmental Microbiology* 81:211–219. https://journals.asm.org/doi/10.1128/AEM.02311-14.

Strathmann, M., T. Griebe, and H. C. Flemming, 2000. Artificial biofilm model- A useful tool for biofilm research. *Applied Microbiology and Biotechnology* 54:231–237. https://link.springer.com/content/pdf/10.1007/s002530000370.pdf.

Burmølle, M., K. Johnsen, W. A. Al-Soud, L. H. Hansen, and S. J. Sørensen, 2009. The presence of embedded bacterial pure cultures in agar plates stimulate the culturability of soil bacteria. *Journal of Microbiological Methods* 79:166–173. http://dx.doi.org/10.1016/j.mimet.2009.08.006.

Zhang, Q., J. Li, J. Nijjer, H. Lu, M. Kothari, R. Alert, T. Cohen, and J. Yan, 2021. Morphogenesis and cell ordering in confined bacterial biofilms. *Proceedings of the National Academy of Sciences* 118. https://pnas.org/doi/full/10.1073/pnas.2107107118.

Cordero, M., N. Mitarai, and L. Jauffred, 2022. Motility mediates satellite formation in confined biofilms. *bioRxiv* 1–12.

Müller, J., A. C. Jäkel, J. Richter, M. Eder, E. Falgenhauer, and F. C. Simmel, 2022. Bacterial Growth, Communication, and Guided Chemotaxis in 3D-Bioprinted Hydrogel Environments. *ACS Applied Materials & Interfaces* 14:15871–15880. https://pubs.acs.org/doi/10.1021/acsami.1c20836.

Eriksen, R. S., S. L. Svenningsen, K. Sneppen, and N. Mitarai, 2018. A growing microcolony can survive and support persistent propagation of virulent phages. *Proceedings of the National Academy of Sciences* 115:337–342. http://www.pnas.org/lookup/doi/10.1073/pnas.1708954115.

Ben-Jacob, E., D. S. Coffey, and H. Levine, 2012. Bacterial survival strategies suggest rethinking cancer cooperativity. *Trends in Microbiology* 20:403–410. http://dx.doi.org/10.1016/j.tim.2012.06.001.

Buffi, N., D. Merulla, J. Beutier, F. Barbaud, S. Beggah, H. van Lintel, P. Renaud, and J. Roelof van der Meer, 2011. Development of a microfluidics biosensor for agarose-bead immobilized Escherichia coli bioreporter cells for arsenite detection in aqueous samples. *Lab on a Chip* 11:2369. http://xlink.rsc.org/?DOI=c1lc20274j.

Kuennen, E. W., and C. Y. Wang, 2008. Off-lattice radial Eden cluster growth in two and three dimensions. *Journal of Statistical Mechanics: Theory and Experiment* 2008:P05014. https://iopscience.iop.org/article/10.1088/1742-5468/2008/05/P05014.

Shao, X., A. Mugler, J. Kim, H. J. Jeong, B. R. Levin, and I. Nemenman, 2017. Growth of bacteria in 3-d colonies. *PLOS Computational Biology* 13:e1005679. https://dx.plos.org/10.1371/journal.pcbi.1005679.

Lavrentovich, M. O., and D. R. Nelson, 2015. Survival probabilities at spherical frontiers. *Theoretical Population Biology* 102:26–39. https://linkinghub.elsevier.com/retrieve/pii/S0040580915000210.

Jullien, R., and R. Botet, 1985. Surface Thickness in the Eden Model. *Physical Review Letters* 54:2055–2055. https://link.aps.org/doi/10.1103/PhysRevLett.54.2055.

Bredenoord, A. L., H. Clevers, and J. A. Knoblich, 2017. Human tissues in a dish: The research and ethical implications of organoid technology. *Science* 355:eaaf9414. https://www.science.org/doi/10.1126/science.aaf9414.

Weiswald, L. B., D. Bellet, and V. Dangles-Marie, 2015. Spherical cancer models in tumor biology. *Neoplasia (New York, N.Y.)* 17:1–15. http://dx.doi.org/10.1016/j.neo.2014.12.004.

Costa, E. C., A. F. Moreira, D. de Melo-Diogo, V. M. Gaspar, M. P. Carvalho, and I. J. Correia, 2016. 3D tumor spheroids: an overview on the tools and techniques used for their analysis. *Biotechnology Advances* 34:1427–1441. http://dx.doi.org/10.1016/j.biotechadv.2016.11.002.

Tomer, R., K. Khairy, F. Amat, and P. J. Keller, 2012. Quantitative high-speed imaging of entire developing embryos with simultaneous multiview light-sheet microscopy. *Nature Methods* 9:755–63. http://www.ncbi.nlm.nih.gov/pubmed/22660741.

Boyer, D., W. Mather, O. Mondragón-Palomino, S. Orozco-Fuentes, T. Danino, J. Hasty, and L. S. Tsimring, 2011. Buckling instability in ordered bacterial colonies. *Physical Biology* 8:026008. https://iopscience.iop.org/article/10.1088/1478-3975/8/2/026008.

Rudge, T. J., F. Federici, P. J. Steiner, A. Kan, and J. Haseloff, 2013. Cell Polarity-Driven Instability Generates Self-Organized, Fractal Patterning of Cell Layers. *ACS Synthetic Biology* 2:705–714. https://pubs.acs.org/doi/10.1021/sb400030p.

Kan, A., I. Del Valle, T. Rudge, F. Federici, and J. Haseloff, 2018. Intercellular adhesion promotes clonal mixing in growing bacterial populations. *Journal of The Royal Society Interface* 15:20180406. https://royalsocietypublishing.org/doi/10.1098/rsif.2018.0406.

Tuson, H. H., G. K. Auer, L. D. Renner, M. Hasebe, C. Tropini, M. Salick, W. C. Crone, A. Gopinathan, K. C. Huang, and D. B. Weibel, 2012. Measuring the stiffness of bacterial cells from growth rates in hydrogels of tunable elasticity. *Molecular Microbiology* 84:874–891. https://onlinelibrary.wiley.com/doi/10.1111/j.1365-2958.2012.08063.x.

Lavrentovich, M. O., J. H. Koschwanez, and D. R. Nelson, 2013. Nutrient shielding in clusters of cells. *Physical Review E* 87:062703. https://link.aps.org/doi/10.1103/PhysRevE.87.062703.

Martínez-Calvo, A., T. Bhattacharjee, R. K. Bay, H. N. Luu, A. M. Hancock, N. S. Wingreen, and S. S. Datta, 2022. Morphological instability and roughening of growing 3D bacterial colonies. *Proceedings of the National Academy of Sciences* 119:819–825. https://pnas.org/doi/10.1073/pnas.2208019119.

Ohgiwari, M., M. Matsushita, and T. Matsuyama, 1992. Morphological Changes in Growth Phenomena of Bacterial Colony Patterns. *Journal of the Physical Society of Japan* 61:816–822. https://journals.jps.jp/doi/10.1143/JPSJ.61.816.

Lavrentovich, M. O., K. S. Korolev, and D. R. Nelson, 2013. Radial Domany-Kinzel models with mutation and selection. *Physical Review E* 87:012103. https://link.aps.org/doi/10.1103/PhysRevE.87.012103.

Dornic, I., H. Chaté, J. Chave, and H. Hinrichsen, 2001. Critical Coarsening without Surface Tension: The Universality Class of the Voter Model. *Physical Review Letters* 87:045701. https://link.aps.org/doi/10.1103/PhysRevLett.87.045701.

Kuhr, J.-T., M. Leisner, and E. Frey, 2011. Range expansion with mutation and selection: dynamical phase transition in a two-species Eden model. *New Journal of Physics* 13:113013. https://iopscience.iop.org/article/10.1088/1367-2630/13/11/113013.

Friedrich, J., C. Seidel, R. Ebner, and L. A. Kunz-Schughart, 2009. Spheroid-based drug screen: considerations and practical approach. *Nature Protocols* 4:309–324. http://www.nature.com/doifinder/10.1038/nprot.2008.226.

Dal Co, A., S. van Vliet, D. J. Kiviet, S. Schlegel, and M. Ackermann, 2020. Short-range interactions govern the dynamics and functions of microbial communities. *Nature Ecology & Evolution* 4:366–375. https://www.nature.com/articles/s41559-019-1080-2.

Borer, B., D. Ciccarese, D. Johnson, and D. Or, 2020. Spatial organization in microbial range expansion emerges from trophic dependencies and successful lineages. *Communications Biology* 3:685. https://www.nature.com/articles/s42003-020-01409-y.

Celik Ozgen, V., W. Kong, A. E. Blanchard, F. Liu, and T. Lu, 2018. Spatial interference scale as a determinant of microbial range expansion. *Science Advances* 4. https://www.science.org/doi/10.1126/sciadv.aau0695.

Monds, R. D., T. K. Lee, A. Colavin, T. Ursell, S. Quan, T. F. Cooper, and K. C. Huang, 2014. Systematic Perturbation of Cytoskeletal Function Reveals a Linear Scaling Relationship between Cell Geometry and Fitness. *Cell Reports* 9:1528–1537. http://dx.doi.org/10.1016/j.celrep.2014.10.040.

Elbing, K., and R. Brent, 2002. Media Preparation and Bacteriological Tools. *Current Protocols in Molecular Biology* 59. https://onlinelibrary.wiley.com/doi/10.1002/0471142727.mb0101s59.

Mao, B., A. Bentaleb, F. Louerat, T. Divoux, and P. Snabre, 2017. Heat-induced aging of agar solutions: Impact on the structural and mechanical properties of agar gels. *Food Hydrocolloids* 64:59–69. https://linkinghub.elsevier.com/retrieve/pii/S0268005X16305793.

Sønderholm, M., K. N. Kragh, K. Koren, T. H. Jakobsen, S. E. Darch, M. Alhede, P. Ã. Jensen, M. Whiteley, M. Kühl, and T. Bjarnsholt, 2017. Pseudomonas aeruginosa Aggregate Formation in an Alginate Bead Model System Exhibits In Vivo -Like Characteristics. *Applied and Environmental Microbiology* 83:1–15. https://journals.asm.org/doi/10.1128/AEM.00113-17.

Kvich, L., B. Fritz, S. Crone, K. N. Kragh, M. Kolpen, M. Sønderholm, M. Andersson, A. Koch, P. Ã. Jensen, and T. Bjarnsholt, 2019. Oxygen Restriction Generates Difficult-to-Culture P. aeruginosa. *Frontiers in Microbiology* 10:1992. https://www.frontiersin.org/article/10.3389/fmicb.2019.01992/full.

Schmid, B., J. Schindelin, A. Cardona, M. Longair, and M. Heisenberg, 2010. A high-level 3D visualization API for Java and ImageJ. *BMC Bioinformatics* 11:274. https://bmcbioinformatics.biomedcentral.com/articles/10.1186/1471-2105-11-274.

Preibisch, S., S. Saalfeld, and P. Tomancak, 2009. Globally optimal stitching of tiled 3D microscopic image acquisitions. *Bioinformatics* 25:1463–1465. https://academic.oup.com/bioinformatics/article/25/11/1463/332497.

Hartmann, R., H. Jeckel, E. Jelli, P. K. Singh, S. Vaidya, M. Bayer, D. K. H. Rode, L. Vidakovic, F. Díaz-Pascual, J. C. N. Fong, A. Dragoš, O. Lamprecht, J. G. Thöming, N. Netter, S. Häussler, C. D. Nadell, V. Sourjik, Ã. T. Kovács, F. H. Yildiz, and K. Drescher, 2021. Quantitative image analysis of microbial communities with BiofilmQ. *Nature Microbiology* 6:151–156. https://www.nature.com/articles/s41564-020-00817-4.

Schindelin, J., I. Arganda-Carreras, E. Frise, V. Kaynig, M. Longair, T. Pietzsch, S. Preibisch, C. Rueden, S. Saalfeld, B. Schmid, J.-Y. Tinevez, D. J. White, V. Hartenstein, K. Eliceiri, P. Tomancak, and A. Cardona, 2012. Fiji: an open-source platform for biological-image analysis. *Nature Methods* 9:676–682. https://www.nature.com/articles/nmeth.2019.

Ollion, J., J. Cochennec, F. Loll, C. Escudé, and T. Boudier, 2013. TANGO: a generic tool for high-throughput 3D image analysis for studying nuclear organization. *Bioinformatics* 29:1840–1841. https://academic.oup.com/bioinformatics/article/29/14/1840/231770.

Sanderson, C., and R. Curtin, 2016. Armadillo: a template-based C++ library for linear algebra. *The Journal of Open Source Software* 1:26. http://joss.theoj.org/papers/10.21105/joss.00026.